Microscopy AND
Microanalysis

Original Article

Improved Protocol for the Quantification of Actinides (Th, U, Np, Pu, Am, and Cm) Using Electron Probe Microanalysis

Xenia Ritter[1,2,†], Philipp Pöml[1]*, Hirokazu Ohta[3], Stéphane Brémier[1], Jérôme Himbert[1], Rachid Hasnaoui[1,‡] and Jasper Berndt[2]

[1]European Commission, Joint Research Centre (JRC), Karlsruhe, Germany; [2]Institut für Mineralogie, Westfälische Wilhelms-Universität Münster, Corrensstr. 24, D-48149 Münster, Germany and [3]Central Research Institute of Electric Power Industry, 2-6-1, Nagasaka, Yokosuka-shi, Kanagawa 240-0196, Japan

Abstract

Measurements of highly radioactive actinides such as Np, Pu, Am, or Cm in as-fabricated or irradiated nuclear fuels are crucial to improve the safety and performance of the nuclear fuel cycle, but also necessary to find solutions to the environmental impact of long-lived actinides in nuclear waste. Currently, the most common technique of measuring the quantity and distribution of actinides in nuclear fuel is electron probe microanalysis (EPMA). However, the accurate analysis of actinides by EPMA is accompanied by numerous obstacles such as interferences in the M-line X-ray region, absorption edges, and the lack of reference materials. Therefore, the measurement protocol of radioactive and irradiated samples requires further investigation and most importantly facilitation. Here, we establish a guideline for precise quantification of actinide elements (Th, U, Np, Pu, Am, and Cm) in fabricated or spent nuclear fuels. For this purpose, we have characterized actinide-bearing reference samples to visualize spectral interferences, list peak, and background positions and employ the standardless calibration curve method for the measurements of Am and Cm. This newly derived analytical protocol was successfully tested on an irradiated fuel sample and can be now implemented as an improved guideline for the quantification of actinides.

Key words: EPMA, M-line interferences, microprobe analysis, minor actinide analysis, nuclear reference materials, post-irradiation examinations

(Received 24 January 2021; revised 6 July 2021; accepted 25 July 2021)

Introduction

Today, 454 active nuclear power plants provide 17.6% of the total worldwide-generated electricity. Although several decommissioning projects have started in the last years due to policy changes, the number of operating reactors is still increasing as a result of worldwide population growth and economic progress (OECD-NEA, 2018). Therefore, considerable research and development is still focused on improving the efficiency of nuclear fuel material and its cycle, but also on finding solutions to reduce the toxicity of long-lived radioactive waste. Studying the distribution and quantity of actinides ($Z = 90$, 92–96) in the fuel after irradiation is of particular interest because actinides are major contributors to the high-level waste but could be potentially reduced through a process called transmutation (Berthou et al., 2003; Fernandez et al., 2009; Ohta et al., 2011; Vespa et al., 2012; Wiss et al., 2014; Capriotti et al., 2017; Wright et al., 2019).

*Corresponding author: Philipp Pöml, E-mail: philipp.poeml@ec.europa.eu
†Current address: Center for Translational Data Science, University of Chicago, 5454 South Shore Drive, Chicago, IL 60615, USA.
‡Current address: Parlement européen, 1, avenue du Président Robert Schuman, F-67070 Strasbourg Cedex, France.

Perhaps the most important nondestructive micro-analytical method that is used to improve the safety and performance of nuclear fuels with the potential of reducing high-level waste is electron probe microanalysis (EPMA) (Walker, 1999; Brémier et al., 2003, 2016; Lamontagne et al., 2007; Walker et al., 2012; Bottomley et al., 2014; Capriotti et al., 2014; Moy et al., 2014; Wiss et al., 2017; Gerczak et al., 2018; Llovet et al., 2020). EPMA is a fast and reliable tool usually applied to earth and material sciences, yet encounters several technical obstacles in nuclear fuel analysis. First, the preparation and characterization of radioactive samples requires specifically designed equipment in nuclear-grade facilities to avoid contamination, such as glove boxes under different atmospheres, under pressure in laboratories, remote handling in hot cells, or lead walls protecting analytical measurement tools and personnel (Walker, 1999). These facilities are globally rare, while research and development on nuclear fuels is strictly regulated by (inter)national policies. Second, microprobe counting detectors and other sensitive parts in the column are exposed to high β- and γ-irradiation from the samples, which demands special and costly shielding (Walker, 1999; Lamontagne et al., 2007; Walker et al., 2012). Third, well-polished surfaces are crucial for the quality of quantitative analysis using EPMA, yet all of the common sample preparation steps such as embedding, grinding, polishing, and controlling the polishing status under a microscope have to be carried out in glove boxes (Walker, 1999;

CrossMark

Lamontagne et al., 2007; Wright et al., 2018), but these "simple" steps are not necessarily available all in one glove box. Thus, every approach in sample transportation imposes a risk of destroying or even losing the sample. These obstacles during preparation for microanalysis occur next to complications in fabrication methods (Wright et al., 2018) or policy and logistical issues during transportation.

Beside all practical and technical complications, EPMA on actinide-bearing samples is an analytical challenge: First, the analysis of the M line region is highly complex. The characteristic main M-line X-rays from the actinides all fall into a narrow energy region (2.8–4 keV), which causes substantial interferences. Second, the Ar K absorption edge at 3.2029 keV occurs in this energy range and reduces the intensity of some actinide element X-ray lines. Moreover, the analysis using M-lines is impaired with uncertainties in mass absorption coefficients (MACs) and lower fluorescence yields compared to K-lines, where the lower fluorescence yields worsen peak-to-background ratios and detection limits (Rinaldi & Llovet, 2015; Pöml & Llovet, 2020). Third, high beam currents (in the hundreds nA) are used to improve counting statistics, which increase the beam size and thus decrease spatial resolution. This trade-off is especially prominent for instruments using W filaments, and it is less problematic for LaB_6/CeB_6 sources and no issue for field emission guns. Note, there are no shielded microprobes using field emission guns to this date. High acceleration voltages of 25 keV are necessary to bypass oxidized layers of samples with high masses ($Z = 90$–96) and advance good statistics of generated X-ray photons in the M line region (2.8–4 keV), but high voltages increase absorption effects, decrease spatial resolution, and excite high-energy L-lines, which in turn can travel long distances in matter and cause fluorescence, including secondary fluorescence across grain boundaries. Thus, the measurement of actinide-containing samples using EPMA remains challenging and requires further investigation and most importantly facilitation.

For this purpose, we report here a step-by-step guideline to quantify actinides (Th, U, Np, Am, Pu, Am, and Cm) in as-fabricated or irradiated nuclear fuels. For the development of this guideline, we have first assessed the status, composition, and homogeneity of rare actinide-bearing reference materials available at the Joint Research Centre of the European Commission (JRC), Karlsruhe, Germany, as the accuracy of any future quantification of unknown samples relies on the accuracy of the measurements on the reference materials. These reference materials were then used to investigate and visualize prominent X-ray interferences in the M-line region and outline the frequently used method to account for interferences. We then define the preferred choice of X-ray lines, list their peak positions, the preferred background positions, and apply the to-date most effective background correction tool (Jercinovic et al., 2012; Allaz et al., 2019). Finally, we use the correction factor approach to quantify the Am and Cm contents for the case where reference samples are not available. The new guideline was successfully tested on an irradiated sample, showing that the measurement of actinides is complex yet achievable. This work should improve the routine post- or prior-irradiation analysis of actinides bearing materials using a shielded electron microprobe.

Materials and Methods

Five actinide reference materials ($<2 \times 1 \times 0.2$ mm) were investigated in this study: in-house prepared powder ceramics of UO_2, PuO_2, and $(U_{0.8}Am_{0.2})O_2$ (Vespa et al., 2012), an in-house prepared single crystal of NpO_2, and a commercially available reference of ThO_2 (Astimex). The in-house prepared samples were cut, polished, and Al-coated ($\sim$20 nm) in glove boxes at JRC Karlsruhe, Germany (Ritter, 2015).

Analysis was carried out using a shielded electron microprobe CAMECA SX 100 R at the JRC Karlsruhe, with four vertically aligned spectrometers, two equipped with $10\bar{1}1$ quartz (QTZ; $2d = 6.686$ Å) and two with pentaerythritol (PET; $2d = 8.742$ Å) crystals for the analysis of actinides. The spectrometers' flow-through proportional counters for PET and QTZ crystals are utilizing P10 as counting gas atmosphere at atmospheric pressure and 2 bars, respectively. Analytical measurement conditions are summarized in Table 1.

Because of the lack of secondary standards, the standards were measured against themselves. For $(U_{0.8}Am_{0.2})O_2$, UO_2 was used for U, NpO_2 was used for Np, and a virtual standard was used for Am (calibration curve approach, see section "Correction factors for missing reference materials: Americium and Curium"). Ten to eleven points were measured on each standard. For ThO_2, no extra standard measurements were performed, and the average of the measurements was taken as the reference value. The measurements on ThO_2 were performed at 20 nA. UO_2 and NpO_2 were measured at 60 nA (standard and unknown points), and 20 nA was used for the PuO_2 reference points, and 180 nA was used for the PuO_2 unknown points.

A shielded microprobe differs from a normal one mainly by shielding the P10 gas flow-through proportional counters from the gamma radiation of the sample using heavy metal such as Pb or W. In addition, the microprobe is usually placed behind a lead wall or inside a lead cell to protect the operator from the radiation. At JRC Karlsruhe, this lead cell has a wall thickness of about 10 cm and is designed to shield about 2 Ci (Walker, 1999; Pöml et al., 2010). The software package "Probe for EPMA" (www.probesoftware.com) was used for acquisition and data processing. For the matrix correction, the PAP model (Pouchou & Pichoir, 1984, 1991) was applied. The MACs of Farthing & Walker (1990) were used. They are based on the equations from Heinrich (1986) with minor modifications and were extrapolated for elements up to Cm.

Results

Reference Material Homogeneity

To assess the homogeneity, status (porosity and planeness), and composition of the reference materials, secondary electron (SE) and backscattered electron (BSE) images, qualitative X-ray maps, and quantitative spot analysis (50–200 spots per reference) were obtained by applying the analytical conditions, as shown in Table 1. For the spot analyses, ThO_2, UO_2, PuO_2, and NpO_2 were used as reference materials for the measurements of Th, U, Pu, and Np, respectively. By using the same reference materials as unknown samples and references alike, that is measuring the reference materials and using the reference as standard material, along with calculating mean, standard deviation, and minimum/maximum of the resulting spot analyses (Table 2), we were able to evaluate the relative composition and homogeneity of the reference materials. Thus, the given weight percent results in Table 2 do not represent absolute values.

As seen in Figure 1 and Table 2, UO_2, NpO_2, and PuO_2 are dense and show good homogeneity. UO_2 and NpO_2 show no porosity, whereas differences in polishing quality can be observed.

Table 1. Analytical Conditions Used for the Measurement of Reference Materials.

	Acceleration Voltage (keV)	Beam Current (nA)	Time on Peak (s)	Time on Background (s)
SE/BSE imaging	15	05/10		
WD spectra[a]	25	20	5[a]	
X-ray maps	25	200	0.2	0.02
Quantitative spot analysis[b]	25	60, 180[c]	40	2 × 10[d]

[a]Dwell time for wavelength-dispersive spectra described as measurement time on peak.
[b]Spot sizes were 1 μm for spot analysis and 20 μm for wavelength-dispersive spectra.
[c]PuO_2.
[d]Two background positions on each side of the peak.

Table 2. Quantitative Spot Analysis Results of Reference Materials Used in This Study Using the Analytical Conditions in Table 1.

[wt.%]	ThO_2 (n = 50)		UO_2 (n = 220)		NpO_2 (n = 208)		PuO_2 (n = 211)			$(U_{0.8}Am_{0.2})O_2$ (n = 293)			
	Th	Total	U	Total	Np	Total	Pu	Am	Total	U	Am	Np	Total
Mean	87.9	100.0	88.1	100.0	88.2	100.1	86.8	0.6	99.1	69.6	16.3	0.6	98.4
RSD (%)	1.3	1.3	0.3	0.2	0.6	0.6	1.0	3.1	0.9	4.0	9.6	44.0	1.6
SE ϵ_k (%)	0.5		0.2		0.2		0.2	2.4		0.2	0.7	4.5	
Minimum	85.2	97.0	87.3	99.2	86.0	97.9	83.9	0.5	96.2	59.9	8.9	0.3	93.5
Maximum	91.1	103.7	88.6	100.5	90.5	102.4	89.1	0.6	101.4	80.0	24.7	3.6	101.9

The following matrix-matching reference materials were used for quantitative spot analysis: commercial ThO_2, in-house prepared UO_2, PuO_2, NpO_2, and a correction factor for AmO_2 (section "Correction factors for missing reference materials: Americium and Curium"). Thus, measured weight percent results do not represent absolute values.
RSD, relative standard deviation; SE, standard error in the intensity ratio (k). Nominal weight percent: 87.9 for Th in ThO_2, 88.2 for U in UO_2, 88.1 for Np in NpO_2, 88.4 for Pu in PuO_2, and 70.3 for U and 17.9 for Am in $U_{0.8}Am_{0.2}O_2$. Totals were obtained by calculating the O contents by stoichiometry (not shown in the table).

The commercially available ThO_2 consists of various pieces, where some show increased porosity. Spot analysis results show slightly higher statistical scattering and we have observed strong electrostatic charging on the ThO_2, and thus, no qualitative maps were acquired for the latter. PuO_2 shows increased porosity and one location around a larger pore (Fig. 1k) with decreased Pu Mα and increased Am Mα intensity. The latter can be either explained by contamination during mixing of the starting material or inhomogeneous mixing of the starting material before/during sintering. Note that the total for PuO_2 is slightly low (99.11 wt %). We attribute that to dead-time issues, because the PuO_2 points were measured at 180 nA in order to properly detect the Am in the PuO_2 reference material.

The $(U_{0.8}Am_{0.2})O_2$ reference material shows increased inhomogeneity including Np impurities and was thus rated unsuitable as a reference material for the routine analysis work at JRC Karlsruhe. Nevertheless, for this work we have used the $(U_{0.8}Am_{0.2})O_2$ reference material for further studies, specifically for the measurement of wavelength-dispersive spectra to observe Am X-ray lines (see following sections).

Line Interferences

Wavelength-dispersive spectra were recorded for peak and interference identification and the selection of background positions on all five reference materials containing Th, U, Np, Pu, and Am, between 2.3 and 7.3 keV (1.7 and 5.4 Å). Figure 2 shows all carefully assessed X-ray lines of Th, U, Np, Pu, and Am measured on ThO_2, UO_2, NpO_2, PuO_2, and $(U_{0.8}Am_{0.2})O_2$, respectively, where the typical spectral background trend can be observed. Peak positions were assessed by manually finding the

highest intensity and recording the spectrometer position. The count rate of the highest-intensity X-ray lines decreases as expected in the following order: Mα>Mβ>Mγ (Fig. 2a). Interestingly, the minimum intensity signal between Mα and Mγ is stronger than the bremsstrahlung continuum due to the overlap of the tails of these peaks. Peaks of rarely seen line transitions such as M_1N_2, M_3O_1, and M_4O_2 are noticeable and show that care must be taken when background positions are selected (see below and section "Background correction and peak positions").

In the next step, these spectra were used to illustrate the complex and convoluted M-line region with all possible interferences between the most common high-intensity peak assemblages (Mα, Mβ, Mγ) of Th, U, Np, Pu, Am, and Cm (Kleykamp, 1991) in Figures 3 and 4. The most prominent interferences occur between U Mα and Th Mβ, Pu Mα, and U Mβ, and between Cm Mα and Am Mβ, yet interferences between low-intensity peaks should not be underestimated. Figure 4 shows a detailed view on the convolution of the M line region. An overview of possible interferences of Mα, Mβ, and Mγ X-ray lines on peak and on background positions (more discussion in section "Background correction and peak positions") is listed in Table 3 and can be used to facilitate the set-up of the analytical protocol. Depending on the elements in the sample, the X-ray lines with the least interferences should be selected for on-peak counting in quantitative spot analysis. Lines with high count rates should, however, be preferred over lines with low count rates—a trade-off. If interferences cannot be avoided, an overlap correction has to be applied: for instance, if the measured line on an unknown sample is U Mα, and Th Mβ is the interfering line, the U Mα intensity has to be corrected for the Th Mβ intensity by measuring the intensity of U Mα on a
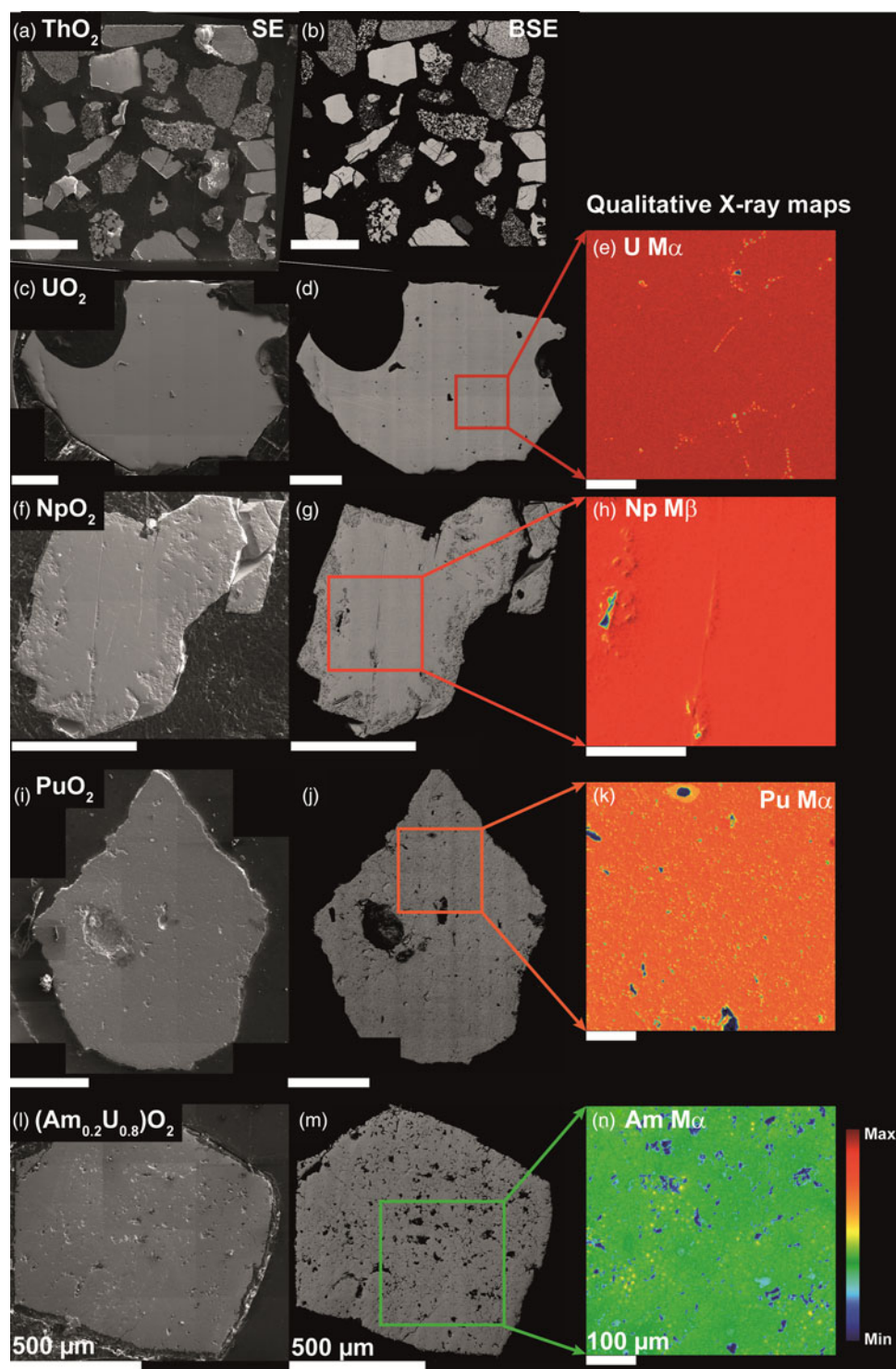
Fig. 1. Secondary electron images (SE, left column) (**a,c,f,i,l**), backscattered electron images (BSE, center column) (**b,d,g,j,m**), and qualitative X-ray maps (right column) (**e,h,k,n**) on the reference materials used in this study (measured X-ray line indicated). Due to too strong electrostatic charges despite Al-coating, a qualitative map was not recorded for ThO_2.

U-free Th reference material (e.g., ThO_2). This intensity should then be subtracted from the U Mα intensity measured on the unknown. Note that this method of overlap correction is a commonly accepted method in EPMA. We want to emphasize that there may not be a one-method-fits-all solution, as discussed in section "Case study on an irradiated sample."

Background Correction and Peak Positions

The spectra shown in section "Line interferences" were used to identify the peak positions from all major observed X-ray lines, which are reported in Table 4. Peak positions were found as the value on the *x*-axis with the maximum intensities on the *y*-axis.
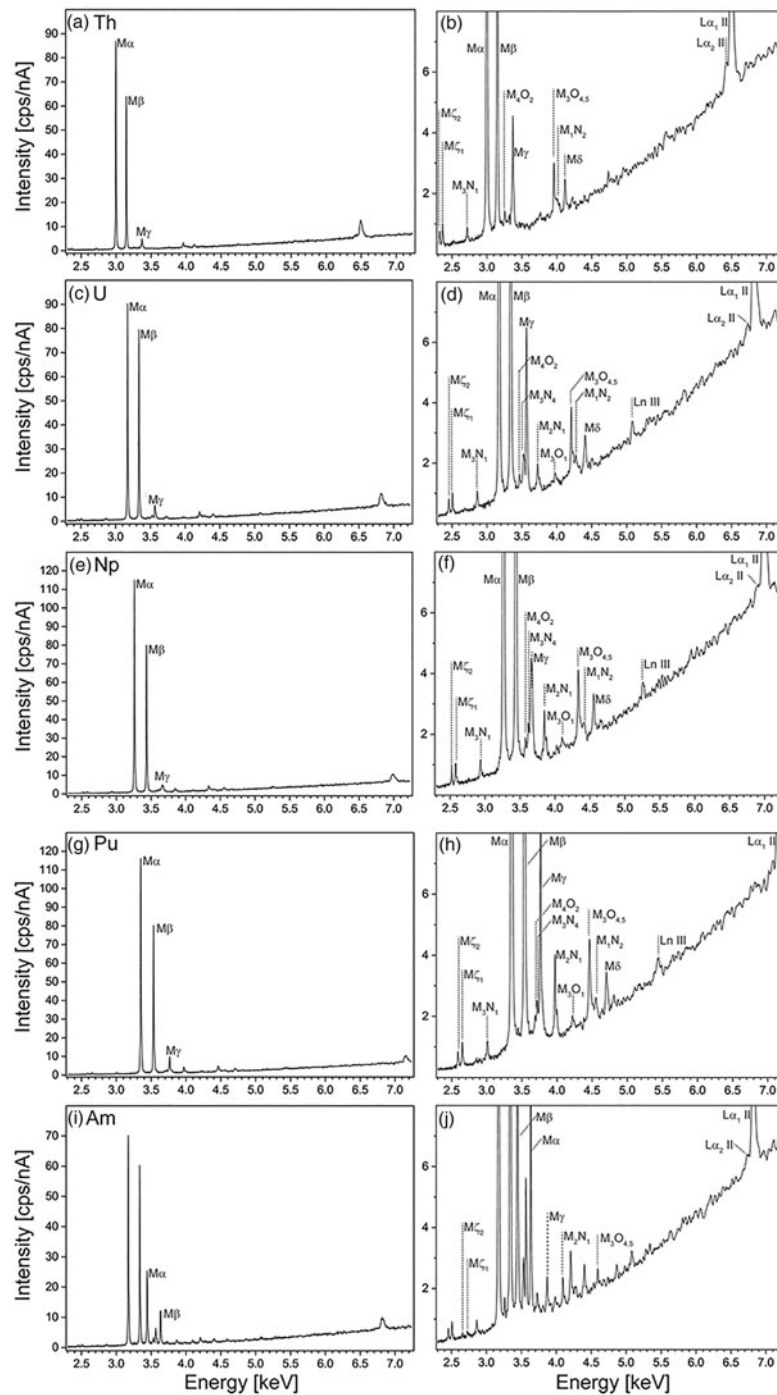
Fig. 2. Detailed wavelength-dispersive spectra measured on QTZ 10-11 showing all high intensity (**a,c,e,g,i**) and respective low intensity (**b,d,f,h,j**) peaks of Th (**a,b**), U (**c,d**), and Np (**e,f**), Pu (**g,h**), and Am (**i,j**). Note the U peaks in **i** and **j**, since the material is $U_{0.8}Am_{0.2}O_2$.

Error (standard deviation) on peak positions is below 1%, as calculated from three wavelength-dispersive spectra reported in a previous study (Ritter, 2015). The energy of U Mα was used to calibrate the spectrometers, as this energy should be reasonably well known. The listed peaks show very good agreement with values previously reported in the literature (Bearden, 1967; Kleykamp, 1981; Dellith et al., 2011; Saber et al., 2014). For instance, Th Mβ lies at 3.145 keV in this study and at 3.145 keV in Bearden (1967); U Mδ lies at 4.402 keV in this study and at 4.402 keV in Dellith et al. (2011); and Pu Mα lies at 3.350 keV in this study and at 3.349 keV in Kleykamp (1981).

However, the Ar K absorption edge (discussed in the following section "Effects from the Ar K absorption edge"), interferences, and increased background signal make it difficult to measure the true background signals of the analytical X-ray line of interest. Using the common background correction approach of selecting one background position close to the peak at each side can lead to significant errors (Allaz et al., 2019), especially if several
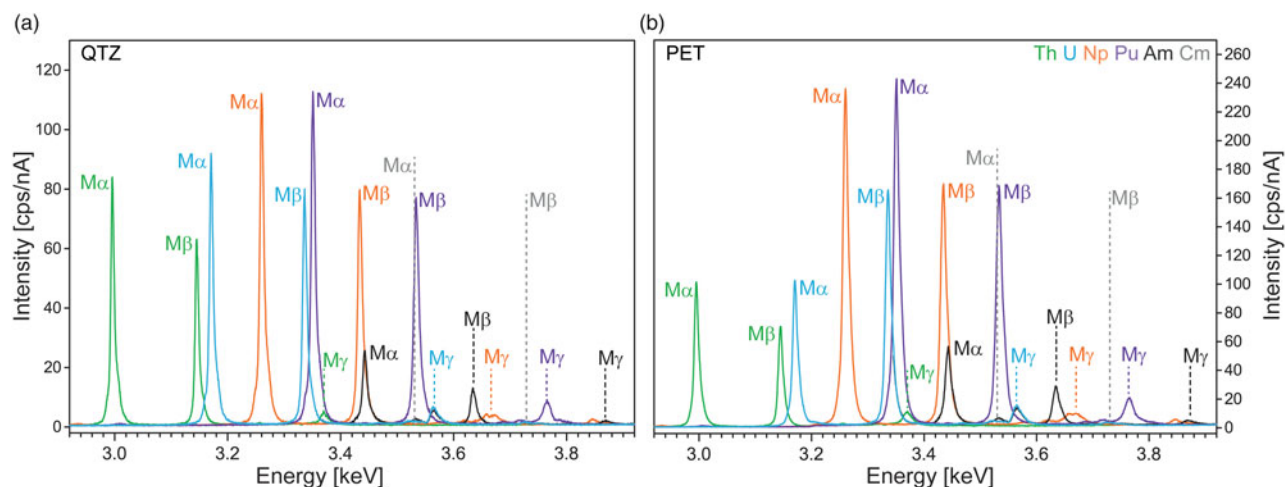
Fig. 3. M-line region of actinides, measured on actinide bearing materials using α-quartz "QTZ" (**a**) (reflecting plane 10$\bar{1}$1, 2d = 6.686 Å) and PET (**b**) (2d = 8.742 Å). Peak assemblages of X-ray M line transitions (α, β, and γ) and the interferences of all measured actinides (Th, U, Np, Pu, and Am) are illustrated. Additionally, peak positions of Cm Mα and Cm Mβ are indicated (Kleykamp, 1991). Note the drop in intensity on the spectrum measured on PET at energies of <3.22 keV as a result from the Ar K absorption edge (see section "Effects from the Ar K absorption edge").
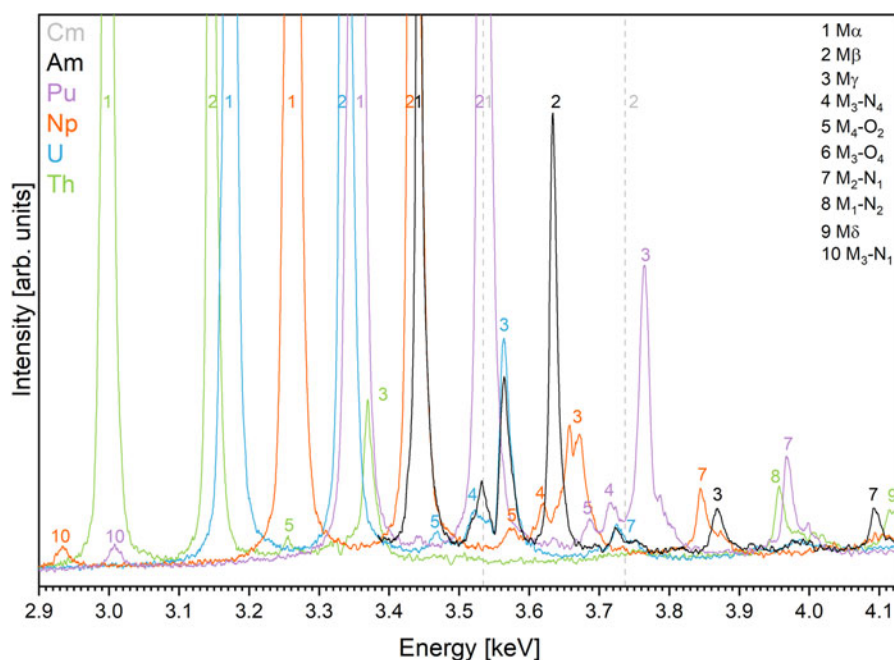

Fig. 4. The complex M-line region from Figure 3 seen here in detail, showing interferences between low-intensity peaks (indicated in numbers). Note that U peaks occur both in U and (U, Am) containing samples. Peak positions of Cm Mα and Cm Mβ (gray, dashed) taken from Kleykamp (1991).

actinides have to be measured in one sample. Thus, we have followed the multi-point background acquisition method (Jercinovic et al., 2012; Allaz et al., 2019), which was initially developed for precise and accurate analysis of transition elements at low concentrations (Merlet & Bodinier, 1990; Jercinovic et al., 2012, 2008). This tool is implemented in the *Probe for EPMA software* package (http://www.probesoftware.com/) and enables the measurement of multiple background points on either side of the peak followed by automatic evaluation and regression. This method significantly improves the background measurement in EPMA, as it allows modeling the "true" background spectrum and gives details about background interferences, holes in the background, or

absorption edges, which can alter the results if neglected (Allaz et al., 2019). Moreover, this tool provides the option to model the background of several elements simultaneously, if elements are analyzed on the same spectrometer (Allaz et al., 2019). This "shared background approach" allows the identification of absorption spectra and interferences during post-processing and reduces measurement times while accurately determining curvature and improving counting statistics (Allaz et al., 2019). Despite its advantages, the operator has to compromise at times between selecting multiple background points and only two background points due to substantially disturbed background signals close to the peaks of interest (see section "Case study on an irradiated sample").

Table 3. Interferences on Peak and Both Background Positions for α, β, and γ X-Ray Lines for Th, U, Np, Pu, Am, and Cm.

Line	On Peak	Higher Energy Background	Lower Energy Background
Th Mα	Pu M_3N_1, Np M_3N_1		Np M_2N_1
U Mα	Th Mβ	Np Mα, Th M_4O_2, Ar K absorption edge	
Np Mα	Th M_3N_4, Th M_4O_2	U Mβ, Pu Mα, Th Mγ	U Mα, Th Mβ
Pu Mα	U Mα, Th Mγ, Th M_3N_4	Np Mβ, Am Mα	Np Mα, Th M_4O_2, Ar K absorption edge
Am Mα	Np Mβ, U M_4O_2, Th Mγ	U Mγ, Pu Mβ, U M_3N_4	Th Mγ, Pu Mα, U Mβ
Cm Mα	Pu Mβ, U M_3N_4		
Th Mβ	U Mα	Ar K absorption edge, Th M_3N_4	
U Mβ	Pu Mα, Th Mγ, Th M_2N_4	Np Mβ, Am Mα, U M_4O_2	Np Mα, Th M_4O_2, Ar K absorption edge
Np Mβ	Am Mα, U M_4O_2	Pu Mβ, U M_3N_4, U Mγ	Th Mγ, Pb Mα, U Mβ, Th M_3N_4
Pu Mβ	U Mγ, U M_3N_4, Np M_4O_2	Np Mγ, Am Mβ	Am Mα, Np Mβ, U M_4O_2
Am Mβ	Np Mγ, Np M_3N_4	Pu Mγ, Np Mγ, Pu M_3N_4, Pu M_4O_2, U M_2N_1	Np M_4O_2, U Mγ, Pu Mβ, U M_3N_4, U M_4O_2
Cm Mβ	Pu Mγ, Pu M_3N_4		
Th Mγ	Pu Mα, U Mβ	Np Mβ, Am Mα, U M_4O_2	Th M_3N_4, Th M_4O_2 Np Mα
U Mγ	Pu Mβ, Np M_4O_2	Am Mβ, Np Mγ, Np M_3N_4	U M_3N_4, U M_4O_2, Pu Mβ, Am Mα, Np Mβ
Np Mγ	Pu M_4O_2, Am Mβ, Np M_3N_4	Pu Mγ, Pu M_3N_4, Pu M_4O_2	Np M_4O_2, Np M_3N_4, U Mγ, Pu Mβ, U M_3N_4
Pu Mγ	Pu M_3N_4, U M_2N_1	Am Mγ, Np M_2N_1	Np Mγ, Np M_3N_4, Pu M_4O_2, Am Mβ
Am Mγ	Np M_2N_1	Pu M_2N_1, Th M_1N_2	Pu Mγ, U M_2N_1, Pu M_3N_4
Cm Mg			

Higher/lower represent higher/lower energy side, respectively. See more details in sections "Line interferences" and "Background correction and peak positions."

Table 4. Peak Positions Determined in This Study (in keV) from Wavelength-Dispersive Spectra Measured on Reference Materials Compared with the Literature.

	Th		U			Np			Pu		Am	
Transition	Bearden (1967)	This Work	Kleykamp (1981)	Dellith et al. (2011)	This Work	Kleykamp (1981)	Saber et al. (2014)	This Work	Kleykamp (1981)	This Work	Kleykamp (1981)	This Work
Lα$_1$ II	—	6.495	—		6.818	—		6.987	—	7.153	—	—
M_2N_4 (δ)	4.117	4.116	4.397	4.402	4.402	4.552		4.553	4.694	4.702	4.852	—
M_1N_2	—	3.995	4.264	4.277	4.270	—		4.410	—	4.560	—	—
$M_3O_{4,5}$ (ε)	3.959	3.958	4.201	—	4.206	4.331		4.333	4.454	4.461	4.584	4.588
M_3O_1	3.776	—	—	3.981	3.990	—		4.095	—	4.219	—	—
M_2N_1	3.505	—	3.721	3.726	3.726	3.847		3.847	3.964	3.969	4.091	4.094
M_3N_5 (γ1)	—	3.369	3.563	3.562	3.564	3.660	3.666	3.664	3.762	3.765	3.867	3.868
M_3N_4 (γ2)	3.334	3.338	3.522	3.522	3.528	3.619		3.620	3.715	3.717	3.815	—
M_4O_2	3.255	3.248	3.466	3.468	3.468	—		3.574	3.687	3.686	—	—
M_4N_6 (β)	3.145	3.145	3.336	3.337	3.336	3.436	3.436	3.434	3.532	3.533	3.632	3.634
M_5N_7 (α1)	2.996	2.995	3.170	3.171	3.171	3.262	3.263	3.260	3.349	3.350	3.441	3.442
M_3N_1	2.714	2.721	2.863	2.862	2.860	2.941		2.932	3.007	3.008	3.082	3.083
M_5N_3 (ζ1)	2.363	2.363	2.508	2.507	2.507	2.580	2.579	2.579	2.653	2.652	2.729	2.728
M_4N_2 (ζ2)	2.321	2.322	2.455	2.455	2.455	2.523	2.520	2.521	2.591	2.589	2.659	—

Errors on peak positions from this work are below 1%, calculated as standard deviation from three measured wavelength-dispersive spectra.

Figure 5 plots an example of how background positions were selected for all actinide elements on reference materials consisting of only one actinide element or two for (U,Am) bearing samples. From this sample, it becomes evident that even samples containing only one actinide element (i.e., Pu), the background curvature is strongly influenced by interferences. After statistical smoothing, two background points were chosen on the lower energy and two on the upper energy range far away from the M-line peak of interest,
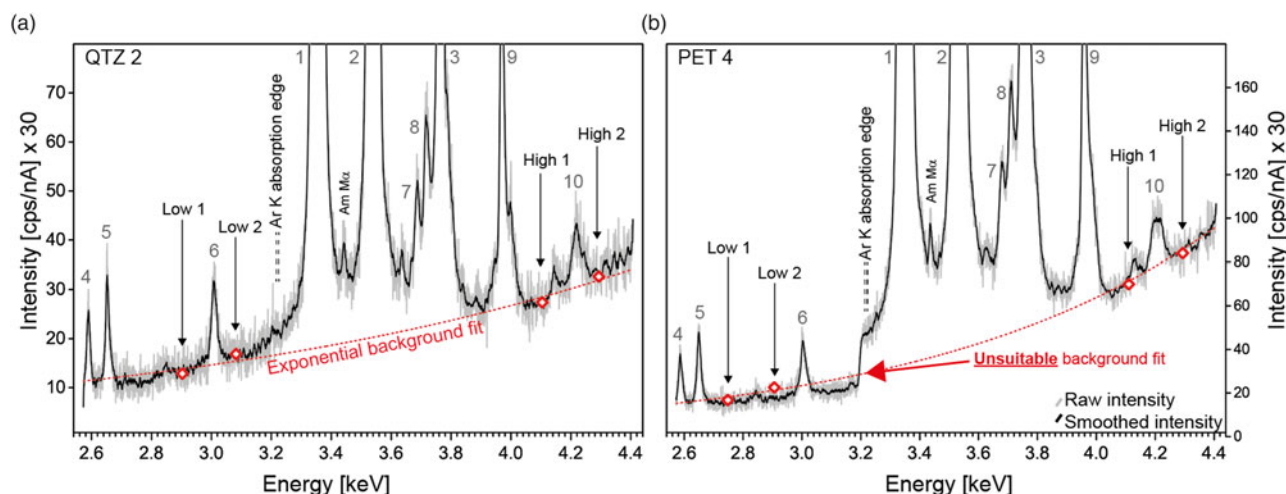
Fig. 5. Wavelength-dispersive spectra measured on the PuO₂ reference material on (**a**) QTZ and (**b**) PET with selected background positions (Low 1,2; High 1,2) for Pu. Interferences occur between Mα, Mβ, and Mγ peaks. The strong Ar K absorption edge effect renders the PET crystal practically unusable, while the effect is hardly seen on the QTZ crystal; see text for explanation. The Am Mα peak appears between Pu Mα and Pu Mβ due to the decay of ^{241}Pu into ^{241}Am ($t_{1/2}$ 14.3a). 1 = Mα, 2 = Mβ, 3 = Mγ, 4 = Mζ_2, 5 = Mζ_1, 6 = M_3N_1, 7 = M_4O_2, 8 = M_3N_4, 9 = M_2N_1, 10 = M_3O_1.

avoiding the Ar-absorption edge, the increased intensity region between the Mα and M_2N_1 peaks (section "Line interferences"), and other interfering low-intensity X-ray lines (Fig. 4). Note the explanations of the Ar K edge effect in Figure 5b in the following section. Fitting the intensity measured on the background positions to an exponential function better represents the continuum spectrum compared to previously overestimated background signals (Reed, 1975, 1997). Following this approach, background positions for all elements were selected and are listed in Table 5.

Effects from the Ar K Absorption Edge

In addition to the interferences, the Ar K absorption edge falls exactly into the energy region of the actinides, causing a sharp intensity drop at 3.2029 keV on the PET crystal. Figure 5b illustrates the effect of the absorption edge on the spectrum measured on PuO₂. The absorption edge lowers the X-ray line intensities and background of the lower-energy side of this edge, and thus intensities of U Mα, Th Mα, Th Mβ, and any background intensities can be significantly lower compared to the X-ray intensities on the higher-energy side, that is, Np Mα or Pu Mα. Note that the low Am Mα intensity is the result of the lower Am content in the reference sample, where (U$_{0.8}$Am$_{0.2}$)O₂ is composed of 6.67 mol% Am compared to 33.34 mol% Np found in NpO₂.

Interestingly, the absorption edge has a significantly higher effect on the PET (Fig. 5), the reason for this being the difference

in gas pressure in the spectrometer's counter. In most flow-through counters installed in EPMA spectrometers "P10" gas, a mixture of 90% Ar and 10% methane is used as the counting gas. The PET crystal is installed in a spectrometer, where the P10 gas in the counter is at atmospheric pressure. In comparison, the QTZ crystal is installed in a spectrometer, where the P10 gas in the counter is at 2 bars pressure. The higher pressure P10 gas shows a relatively small effect of the Ar K absorption edge, and the QTZ offers a *slightly* better energy resolution than the PET; that is, the full width at half maximum of the Pu Mα peak on the QTZ is 0.0107278 and 0.0120292 on the PET using a Voigt fit function. Thus, QTZ is the preferred choice for the measurement of actinides, as it resolves the line overlaps better. In fact, the strong Ar K edge effect on the atmospheric pressure spectrometer using the PET renders this setup virtually unusable. It is hence necessary to have either a QTZ or a PET crystal installed on a high-pressure spectrometer to properly measure the actinide M-lines. Alternatively, to avoid the side effects of the Ar absorption edge, sealed xenon counters could be used, but these are not available for the EPMA model used in this study.

Correction Factors for Missing Reference Materials: Americium and Curium

If reference materials are not available, other methods can be used to quantify the concentrations of an element. First, standardless

Table 5. Complete set of Background Positions (in keV, sinΘ, and mm) for Mα X-Ray Lines for Th, U, Am, Np, and Pu, to Be Used for Reference Materials Consisting of One Actinide Element.

Crystal (sp)	Element	keV (Energy)				sinΘ (Cameca Units)				mm (JEOL Units)			
		Low 1	Low 2	High 1	High 2	Low 1	Low 2	High 1	High 2	Low 1	Low 2	High 1	High 2
QTZ	Th	3.860	3.621	2.809	2.604	48,028	51,192	66,000	71,200	134.5	143.3	184.8	199.4
QTZ	U/Am	4.156	4.043	2.804	2.605	44,600	45,855	66,100	71,154	124.9	128.4	185.1	199.2
QTZ	Np	4.183	4.005	3.022	2.809	44,320	46,290	61,350	66,000	124.1	129.6	171.8	184.8
QTZ	Pu	4.292	4.104	3.081	2.902	43,186	45,170	60,160	63,877	120.9	126.5	168.4	178.9

or virtual reference procedures are highly promising as reported in Limandri et al. (2012), Trincavelli et al. (2014), Moy et al. (2014, 2015), and Pinard et al. (2020), which are accompanied by an error of 9% for heavy elements (Moy et al., 2014, 2015). Second, specifically for the quantification of Am, a missing reference for Am can be replaced by measuring the Am in-growth in the PuO_2 material. Since ^{241}Pu decays into ^{241}Am with a half-life of $t\frac{1}{2} = 14.3a$, the americium content in the PuO_2 reference of known age could also be calculated and used as a virtual reference (Walker, 1999; Lamontagne et al., 2007, 2013). This method can be used for other elements, where the radioactive decay and half-life are well known. However, it is important to note that the accuracy of this option suffers from low concentrations of the in-growth, which inevitably results in lower counting statistics and thus higher errors in the final results. A third and last option is the derivation of a calibration curve for the missing reference (Walker, 1999; Pöml et al., 2010; Wright & van Rooyen, 2020).

In this study, we found the in-house prepared material $(U_{0.8}Am_{0.2})O_2$ was not suitable to be used as a reference material for Am due to its inhomogeneity. Thus, we followed the third mentioned approach to derive a correction factor for Am Mβ, as an example, by measuring the Mβ intensities of adjacent elements and fitting them to a linear regression. In this way, the U intensity can be used as a reference material for Am. In detail, the Mβ intensities of U, Np, and Pu ($Z = 92-94$) are measured on one spectrometer, for example, on pure metals or oxides, corrected for k-ratio, dead-time, and coating effects, and subsequently normalized to the U Mβ intensity. After Moseley's law, these ratios are plotted as a function of atomic number and fitted to a linear regression (Fig. 6), which is extrapolated using the atomic number of Am to derive the correction factor (Am Mβ/U Mβ ratio) for Am. This factor is then multiplied with the U Mβ standard intensity (metal or oxide) to derive the theoretical intensity of Am in a virtual metal or oxide standard. This linear regression could be further extrapolated to derive a correction factor for Cm Mβ despite an increase in uncertainty, which is the trade-off for not having any physical standard available at all. Figure 6 shows the derivation of the correction factor for Am Mβ and Cm Mβ for each spectrometer. Here, it can be observed that Th Mβ needed to be excluded from the derivation of the calibration curve due to the sharp intensity drop caused by the Ar K absorption edge (Figs. 3, 5, 6; section "Effects from the Ar K absorption edge"). Uncertainties on the extrapolated ratios using the U Mβ intensity as denominator were determined from the 95% confidence limits, resulting in 3.6, 5.8, and 8.2% on Pu, Am, and Cm, respectively.

Similar to the Mβ line regression, the intensities from Mα lines were measured and tested to be used to derive a correction factor for Am or Cm. However, the Ar K absorption edge would affect both Th Mα and U Mα intensities, and as a result, only Np Mα and Pu Mα would be taken into account for the linear regression while using Np Mα as the common denominator (Fig. 6).

It should be stated that the composition of the sample and the resulting interferences should dictate which correction factors should be used, either those derived from Mα or from Mβ lines. For instance, if a sample contains U, Np, Pu, Am, and Cm, the Am concentration should be measured by using the Mα correction factor and the Cm concentration can be measured by using the Cm Mβ correction factor (see section "Case study on an irradiated sample").
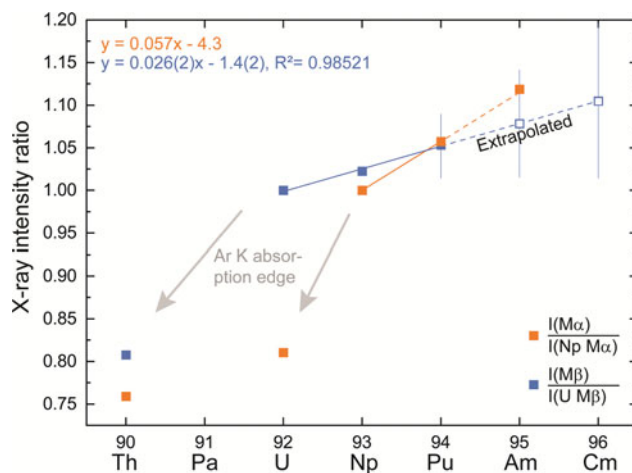

Fig. 6. Measured intensities from which the Am and Cm correction factors were derived using the X-ray intensities of Np Mα (orange) and U Mβ (blue) as common denominator. Note the intensity drop caused by the Ar K absorption edge (indicated as gray arrows) between U Mβ and Pu Mβ and between Th Mα and U Mα. 95% confidence limits are indicated as error bars on extrapolated intensity ratios for one fit; standard errors of the linear fit parameters are indicated in parentheses.

Case Study on an Irradiated Sample

We report the quantitative analysis of an irradiated sample taking into account the analytical guidelines discussed in the previous sections. The sample in this case study is an irradiated metal fuel alloy, its base elements being U, Pu, Zr, minor actinides (Np, Am, and Cm), and rare earth elements (Y, Ce, Nd, and Gd; Capriotti et al., 2017). This sample is part of the METAPHIX program, which is a collaboration between the JRC and the Central Research Institute of Electric Power Industry (CRIEPI, Japan) focused on studying the effectiveness and safety of a closed nuclear fuel cycle with regard to minor actinide separation from spent fuel, incorporation in metal alloy fuel, and transmutation in fast reactors (Ohta et al., 2015; Capriotti et al., 2017). The irradiated sample shows strong porosity and compositionally different areas (Fig. 7). We chose to report results of two distinct areas (Fig. 7), hereafter referred to as Phases 1 and 2. Note that irradiated metallic fuel is prone to fast oxidation in air. To minimize any effects, the sample was prepared under an N_2 atmosphere, coated with 20 nm Al, and then transported under vacuum to the EPMA where it remained under the chamber vacuum during analysis.

In the first step, it is crucial to record energy- or wavelength-dispersive spectra in order to identify elemental sample composition, to observe and avoid possible interferences, and to select X-ray lines and background positions for the quantitative measurement protocol. Note that selecting X-ray lines and background positions while describing interferences go usually hand in hand. Figure 8 shows the wavelength-dispersive spectra of the two different phases measured on the irradiated sample. Individual peaks were modeled with a Voigt function in the *Fityk* software (Wojdyr, 2010) to observe possible interferences. Phase 1 is Am, Cm, and Pu-rich, whereas Phase 2 shows increased concentrations of U, Pu, and Np. The wavelength-dispersive spectra in Figure 8 show that both phases reveal several interferences such as Am Mα with Np Mβ, Pu Mα with U Mβ, as well as Cm Mα with Pu Mβ. Moreover, Figure 8 shows that the L-lines of rare earth elements heavily interfere with the M-lines of minor actinides, and thus need to be corrected on top of the
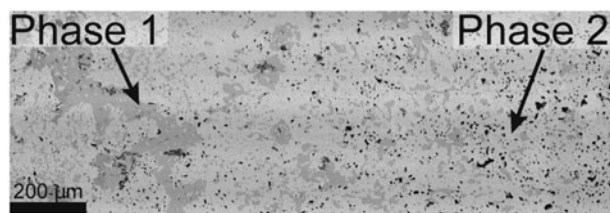
Fig. 7. BSE image of the irradiated fuel, showing the two investigated phases.

minor actinide interferences. For instance, Cm Mβ is corrected for U and Pu, and Pu Mα is corrected for U and Gd (Table 6), similar to what is reported in Wright et al. (2019). It is important to note, however, that with a sample consisting of minor actinides and other transition/rare earth elements ($Z = 57$–71), the operator has to compromise at times that several elements may have to be excluded from the measurement protocol due to the too-strong interferences. For the X-ray lines of both Am and Cm, we selected for this fuel to take Am Mα and Cm Mβ into the measurement protocol. Am Mα was selected due to the high intensity of the Am Mα peak and the low contents of Np. Despite the strong interferences between Cm Mβ and Pu Mγ, Cm Mβ was selected for quantitative spot analysis due to the better linear fit in the calibration curve derivation (Fig. 6).

Figures 2–4 and Table 3 are further used to select X-ray lines with the least interferences. Table 6 then summarizes the measurement protocol including X-ray lines, reference materials (see more information below), spectrometer crystals, respective peak and background positions, and the respective corrections applied for the occurring interferences, as described in the section "Line interferences."

In the next step, reference materials need to be selected. For this metallic fuel specimen, metallic standards were used where possible to avoid large matrix corrections that can occur when using oxide standards for a metallic sample. Unfortunately, for Np and Pu metallic reference materials were not available, and $NpAl_2$ and PuO_2 were used. As for the measurements of Am and Cm, the calibration curve approach was selected (Fig. 6; Table 6). For Am, a virtual metallic standard was created and its Am Mα intensity was calculated from the intensity of Np Mα on $NpAl_2$ using a factor of 1.47. For Cm, a virtual metallic standard was created and its Cm Mβ intensity was calculated from the intensity of U Mβ on metallic U using a factor of 1.1.

Next, the analyzing spectrometer crystals have to be selected. In our case, Quartz was preferred over PET due to higher energy
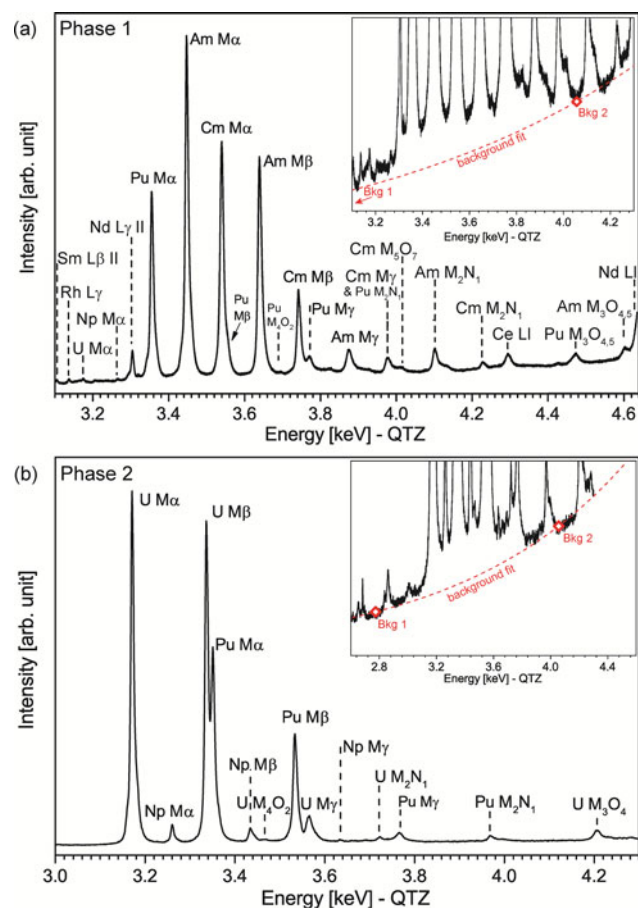

Fig. 8. Wavelength-dispersive spectra measured on two phases present in the irradiated sample. (**a**) shows the Am, Cm, Pu-rich Phase 1, and (**b**) shows the U, Pu, Np-rich Phase 2. Interferences between all elements lead to increased background intensities and asymmetrical peak shapes (Cm Mα and Pu Mβ in (**a**)). Inlet shows modeled background signal. A typical quantitative measurement of each phase is given in Table 7.

resolution for actinides and lower Ar K absorption effect (as discussed in the section "Effects from the Ar K absorption edge"). The next step is to select background positions, for which Tables 3–5 are used as a guideline. As stated above, the background positions were limited by the interferences between L- and M-lines. Therefore, only two background positions were selected far away from the peak convolution and exponentially fitted (Table 6; Fig. 8, inlet). Figure 8 shows that the exponentially

Table 6. Measurement Protocol for the Analysis of an Irradiated Sample, Measured at 25 keV at 250 nA, Using the QTZ Crystal.

X-Ray Line	Peak (keV)	Reference Material	Bkg 1 (keV)	Bkg 2 (keV)	Corrected for
U Mα	3.175	U	2.774	4.057	Pd
Np Mα	3.264	$NpAl_2$[a]	"	"	U
Pu Mα	3.355	PuO_2[a]	"	"	U, Gd
Am Mα	3.447	Virtual metallic standard[b]	"	"	Np, U, Pu[c]
Cm Mβ	3.742	Virtual metallic standard[d]	"	"	U, Pu

Measurement times are 50 s on the peak and 25 s on each background position.
[a]Unfortunately, Np and Pu metal standards were not available.
[b]1.47 using Np Mα on $NpAl_2$ as reference.
[c]Note that the correction for Pu on Am Mα is problematic because the PuO_2 standard contains a minor amount of Am.
[d]1.10 using U Mβ on U for Cm. The correction factor would be 1.08 for Am Mβ.

Table 7. Analysis Conditions, Standardization Details, Interferences/Background Corrections, and Quantitative Spot Analyses (in wt%) of Two Phases of the Irradiated Sample Using the Updated Analytical Protocol.

Element	X-Ray Line	Crystal	Reference Material	Interferences	nA (Reference)	nA (Unknown)	Spot size on Reference (µm)	Time (s) on Reference		Time (s) on Unknown		Results					
								On Peak	Bkg	On Peak	Bkg	Phase 1	DL 99%	SE (%)	Phase 2	DL 99%	SE (%)
Ti	Kα	LiF	Ti		20	250	1	20	20	50	50	n.d.	0.01		0.01	0.01	38
La	Lα	LiF	LaPO$_4$	Nd, Cs	20	250	10	20	20	50	50	1.46	0.07	2.6	n.d.	0.09	
Ce	Lα	LiF	CeF$_3$		20	250	10	20	20	50	50	9.83	0.02	0.3	0.03	0.02	41.5
Pr	Lα	LiF	PrF$_3$	La	20	250	10	20	20	50	50	1.26	0.02	1.1	n.d.	0.02	
Nd	Lα	LiF	NdF$_3$	Ce	20	250	10	20	20	50	50	47.3	0.06	0.1	n.d.	0.07	
U	Mα	QTZ	U	Pd	20	250	1	20	20	50	50	0.07	0.02	14.7	64.1	0.02	0.1
Np	Mα	QTZ	NpAl$_2$	U	20	250	1	20	20	50	50	0.09	0.06	35.6	2.58	0.06	1.2
Pu	Mα	QTZ	PuO$_2$	U, Gd	20	250	1	20	20	50	50	8.84	0.06	0.4	20.0	0.05	0.2
Am	Mα	QTZ	virtual	U, Np, Pu	20	250	1	20	20	50	50	15.1	0.06	0.3	n.d.	0.05	
Cm	Mβ	QTZ	virtual	U, Pu, Ni	20	250	1	20	20	50	50	4.94	0.09	1.1	n.d.	0.12	
Xe	Lα	QTZ	virtual	La, Np	20	250	1	20	20	50	50	0.13	0.01	4.4	0.03	0.02	26.2
Cs	Lβ	LiF	Pollucite	La, Nd	20	250	10	20	20	50	50	0.12	0.03	12.2	n.d.	0.03	
Cr	Kα	LiF	Cr		20	250	1	20	20	50	50	0.01	0.01	54.3	n.d.	0.02	
Fe	Kα	LiF	Fe	Nd	20	250	1	20	20	50	50	n.d.	0.02		0.06	0.02	13.5
Ni	Kα	LiF	Ni	Sm	20	250	1	20	20	50	50	n.d.	0.01		n.d.	0.01	
Y	Lα	PET	Y		20	250	1	20	20	50	50	1.47	0.02	1.1	0.02	0.01	41.9
Zr	Lα	PET	Zr		20	250	1	20	20	50	50	0.1	0.06	30	9.46	0.05	0.4
Mo	Lα	PET	Mo		20	250	1	20	20	50	50	n.d.	0.01		0.73	0.01	1.4
Ru	Lα	PET	Ru		20	250	1	20	20	50	50	n.d.	0.04		0.74	0.04	3
Rh	Lα	PET	Rh	Ru	20	250	1	20	20	50	50	0.01	0.01	58.5	0.09	0.01	7.1
Pd	Lβ	PET	Pd	Y, Rh, Pu	20	250	1	20	20	50	50	n.d.	0.10		0.16	0.09	28
Sm	Lα	LiF	Sm	Ce, Nd	20	250	1	20	20	50	50	1.22	0.01	0.7	0.01	0.01	104.3
Mn	Kα	LiF	Mn	Cr, Pr	20	250	1	20	20	50	50	0.07	0.01	10.5	n.d.	0.02	
Gd	Lα	LiF	Gd	Ce, Nd	20	250	1	20	20	50	50	4.67	0.06	0.8	0.07	0.07	51.3
Total												96.7			98.2		

Phase 1 is minor Actinide and REE-rich; Phase 2 is U and Pu-Rich.
DL, detection limit; SE, standard error; n.d., not detected.

Xenia Ritter et al.

fitted background follows the background signal, yet we want to emphasize that more background positions are the preferred choice for future measurements.

Finally, the new measurement protocol seen in Table 6 was applied to quantitative spot analysis on the two distinct phases. The results of spot analysis of two phases in the irradiated sample are given in Table 7, showing that Phase 1 of this sample contains high amounts of Am (15.1 wt%), Cm (4.94 wt%), and Nd (47.3 wt %) and trace amounts of Np (<0.09 wt%) and U (<0.07 wt%). Phase 2 contains high amounts of U (64.1 wt%), Pu (20 wt%), and Zr (9.46 wt%). The total values of Phases 1 and 2 show 96.7 and 98.2 wt%, respectively, which attest to the reliability of the new and improved guideline to measure actinides in fabricated or spent fuels, despite all above described analytical obstacles. Note that the slightly low total values can be attributed to either sub-micron porosity formed during irradiation or fission products that were not measured in this measurement protocol. In general, a total of 97-98 wt% is excellent for an irradiated fuel specimen.

Conclusion

In this work, we discussed the problems and challenges involved with the analysis of actinide elements using the electron microprobe and provide tools and a guideline for setting up an appropriate analysis protocol. For this purpose, the convoluted and complex region of X-ray lines emitted from the M shells was carefully investigated in order to avoid major interferences, absorption edge effects, and to select preferred peak and background positions. Options to include standardless methods were described for Am and Cm. The new and improved guideline was successfully tested on an irradiated sample, which can now be used as a base protocol for the microanalysis of actinide-bearing samples, for instance during routine post-irradiation examinations. Therefore, despite the encountered obstacles, the electron microprobe remains an important tool to investigate radioactive elements in unknown samples. Future investigations should focus on verifying MACs of actinide elements, for example, by empirical measurements, and strengthening research on standardless approaches.

References

Allaz JM, Williams ML, Jercinovic MJ, Goemann K & Donovan J (2019). Multipoint background analysis: Gaining precision and accuracy in microprobe trace element analysis. *Microsc Microanal* **25**, 30–46.

Bearden JA (1967). X-ray wavelengths. *Rev Mod Phys* **39**, 78–124.

Berthou V, Degueldre C & Magill J (2003). Transmutation characteristics in thermal and fast neutron spectra: Application to americium. *J Nucl Mater* **320**, 156–162. doi:10.1016/S0022-3115(03)00183-1.

Bottomley PDW, Walker CT, Papaioannou D, Bremier S, Pöml P, Glatz JP, Van Winckel S, Van Uffelen P, Manara D & Rondinella VV (2014). Severe accident research at the Transuranium Institute Karlsruhe: A review of past experience and its application to future challenges. *Ann Nucl Energy* **65**, 345–356. doi:10.1016/j.anucene.2013.11.012.

Brémier S, Haas D, Somers J & Walker CT (2003). Large area quantitative X-ray mapping of (U,Pu)O₂ nuclear fuel pellets using wavelength dispersive electron probe microanalysis. *Spectrochim Acta B: At Spectrosc* **58**, 651–658.

Brémier S, Inagaki K, Capriotti L, Poeml P, Ogata T, Ohta H & Rondinella VV (2016). Electron probe microanalysis of a METAPHIX UPuzr metallic alloy fuel irradiated to 7.0 at% burn-up. *J Nucl Mater* **480**, 109–119.

Capriotti L, Brémier S, Inagaki K, Pöml P, Papaioannou D, Ohta H, Ogata T & Rondinella VV (2017). Progress in nuclear energy characterization of metallic fuel for minor actinides transmutation in fast reactor. *Prog Nucl Energy* **94**, 194–201.

Capriotti L, Inagaki K, Papaioannou D, Brémier S, Ohta H, Ogata T, Eloirdi R, Bocci F, Bouëxière D & Rondinella VV (2014). Phase characterization in unirradiated and irradiated metallic fuel for minor actinides transmutation in fast reactor. *Trans Am Nucl Soc* **110**, 781–782.

Dellith J, Scheffel A, Terborg R & Wendt M (2011). Reinvestigation of the M emission spectrum of uranium-92. *Microsc Microanal* **17**, 296–301. doi:10.1017/S1431927611000067.

Farthing IR & Walker CT (1990). Heinrich's mass absorption coefficients (for the K, L, and M X-ray lines). Technical Note K0290140. Commission of the European Communities, Joint Research Centre, Karlsruhe.

Fernandez A, McGinley J, Somers J & Walter M (2009). Overview of past and current activities on fuels for fast reactors at the institute for transuranium elements. *J Nucl Mater* **392**, 133–138. doi:10.1016/j.jnucmat.2009.03.006

Gerczak TJ, Parish CM, Edmondson PD, Baldwin C & Terrani KA (2018). Restructuring in high burnup O₂ studied using modern electron microscopy. *J Nucl Mater* **509**, 245–259. doi:10.1016/j.jnucmat.2018.05.077

Heinrich KFJ (1986). Mass absorption coefficients for electron probe microanalysis. In *11th Congress on X-ray Optics and Microanalysis*, Brown JD & Packwood AH (Eds.), pp. 67–119. London: University of Western Ontario.

Jercinovic MJ, Williams ML, Allaz J & Donovan JJ (2012). Trace analysis in EPMA. *IOP Conf Ser: Mater Sci Eng* **32**, 1–22.

Jercinovic MJ, Williams ML & Lane ED (2008). In-situ trace element analysis of monazite and other fine-grained accessory minerals by EPMA. *Chem Geol* **254**, 197–215.

Kleykamp H (1981). Wavelengths of the M X-Ray spectra of uranium, neptunium, plutonium, and americium. *Zeitschrift für Naturforschung A* **36**, 1388–1390.

Kleykamp H (1991). X-ray emission wavelengths of Argon, Krypton, Xenon, and Curium. *Zeitschrift für Naturforschung A* **47a**, 460–462.

Lamontagne J, Blay T & Roure I (2007). Microbeam analysis of irradiated materials: Practical aspects. *Microsc Microanal* **13**, 150–155. doi:10.1017/S143192760707033X

Lamontagne J, Pontillon Y, Esbelin E, Béjaoui S, Pasquet B, Bourdot P & Bonnerot JM (2013). Determining the americium transmutation rate and fission rate by post-irradiation examination within the scope of the ECRIX-H experiment. *J Nucl Mater* **440**, 366–376. doi:10.1016/j.jnucmat.2013.05.057

Limandri SP, Bonetto RD, Josa VG, Carreras AC & Trincavelli JC (2012). Standardless quantification by parameter optimization in electron probe microanalysis. *Spectrochim Acta Part B At Spectrosc* **77**, 44–51. doi:10.1016/j.sab.2012.08.003

Llovet X, Moy A, Pinard PT & Fournelle JH (2020). Electron probe microanalysis: A review of recent developments and applications in materials science and engineering. *Prog Mater Sci* **116**, 100673. doi:10.1016/j.pmatsci.2020.100673.

Merlet C & Bodinier J-L (1990). Electron microprobe determination of minor and trace transition elements in silicate minerals: A method and its application to mineral zoning in the peridotite nodule PHN1611. *Chem Geol* **83**, 55–69.

Moy A, Merlet C & Dugne O (2015). Standardless quantification of heavy elements by electron probe microanalysis. *Anal Chem* **87**, 7779–7786. doi:10.1021/acs.analchem.5b01443.

Moy A, Merlet C, Llovet X & Dugne O (2014). Optimization of actinide quantification by electron probe microanalysis. *IEEE Trans Nucl Sci* **61**, 1977–1983.

OECD-NEA (2018). 2018 NEA Annual Report.

Ohta H, Ogata T, Papaioannou D, Kurata M, Koyama T, Glatz JP & Rondinella VV (2011). Development of fast reactor metal fuels containing minor actinides. *J Nucl Sci Technol* **48**, 654–661.

Ohta H, Ogata T, Papaioannou D, Rondinella VV, Masson M & Paul JL (2015). Irradiation of minor actinide-bearing uranium-plutonium-

zirconium alloys up to ~2.5 at%, ~7 at%, and ~10 at% burnups. *Nucl Technol* **190**, 36–51.

Pinard PT, Protheroe A, Holland J, Burgess S & Statham PJ (2020). Development and validation of standardless and standards-based X-ray microanalysis. *IOP Conf Ser: Mater Sci Eng* **891**, 012020.

Pöml P, Brémier S, Lahuerte F, Hasnoui R & Walker CT (2010). Calibration of a Cameca SX100 microprobe for the measurement of retained xenon in nuclear fuels. In *11th European Workshop on Modern Developments and Applications in Microbeam Analysis IOP Publishing*. vol. 7, pp. 1–5.

Pöml P & Llovet X (2020). Determination of mass attenuation coefficients of Th, U, Np, and Pu for oxygen Kα X-rays using an electron microprobe. *Microsc Microanal* **26**, 194–203.

Pouchou JL & Pichoir F (1984). Un nouveau modèle de calcul pour la micro-analyse hétérogènes en profondeur. *La Recherche Aérospatiale* **5**, 349–367.

Pouchou JL & Pichoir F (1991). Quantitative analysis of homogeneous or stratified microvolumes applying the model "PAP". In *Electron Probe Quantitation*, Heinrich KFJ & Newbury DE (Eds.), pp. 31–75. New York: Plenum Press.

Reed SJB (1975). The shape of the continuous X-ray spectrum and background corrections for energy-dispersive electron microprobe analysis. *X-Ray Spectrom* **4**, 14–17.

Reed SJB (1997). *Electron Microprobe Analysis*, 2nd ed. Cambridge: Cambridge University Press.

Rinaldi R & Llovet X (2015). Electron probe microanalysis: A review of the past, present, and future. *Microsc Microanal* **21**, 1053–1069. doi:10.1017/S1431927615000409

Ritter X (2015). *Micro-analytical investigations on actinide reference materials*. Westfälische Wilhelms-Universität Münster, Münster.

Saber IA, Chen-Zhong D, Xiang-Li W, Wei-Dong Z & Zhong-Wen W (2014). Theoretical study on K, L, and M X-ray transition energies and rates of neptunium and its ions. *Chin Phys B* **23**, 023101.

Trincavelli J, Limandri S & Bonetto R (2014). Standardless quantification methods in electron probe microanalysis. *Spectrochim Acta Part B At Spectrosc* **101**, 76–85. doi:10.1016/j.sab.2014.07.016.

Vespa M, Rini M, Spino J, Vitova T & Somers J (2012). Fabrication and characterization of (U, Am)O$_{2-x}$ transmutation targets. *J Nucl Mater* **421**, 80–88.

Walker CT (1999). Electron probe microanalysis of irradiated nuclear fuel: An overview. *J Anal At Spectrom* **14**, 447–454.

Walker CT, Brémier S, Pöml P, Papaioannou D & Bottomley PWD (2012). Microbeam analysis of irradiated nuclear fuel. *IOP Conf Ser: Mater Sci Eng* **32**, 1–15. 10.1088/1757-899X/32/1/012028

Wiss T, Hiernaut JP, Roudil D, Colle JY, Maugeri E, Talip Z, Janssen A, Rondinella V, Konings RJM, Matzke HJ & Weber WJ (2014). Evolution of spent nuclear fuel in dry storage conditions for millennia and beyond. *J Nucl Mater* **451**, 198–206. doi:10.1016/j.jnucmat.2014.03.055

Wiss T, Rondinella VV, Konings RJM, Staicu D, Papaioannou D, Bremier S, Pöml P, Benes O, Colle J, Van Uffelen P, Schubert A, Cappia F, Marchetti M, Pizzocri D, Jatuff F, Goll W, Sonoda T, Sasahara A, Kitajima S & Kinoshita M (2017). Properties of the high burnup structure in nuclear light water reactor fuel. *Radiochim Acta* **105**, 893–906.

Wojdyr M (2010). Fityk: A general-purpose peak fitting program. *J Appl Crystallogr* **43**, 1126–1128. doi:10.1107/S0021889810030499.

Wright KE, Harp JM & Capriotti L (2019). Electron probe microanalysis of irradiated FUTURIX-FTA U-Pu-Zr alloy with added minor actinides. *J Nucl Mater* **526**, 151745. doi:10.1016/j.jnucmat.2019.151745.

Wright KE, Popa K & Pöml P (2018). Synthesis and characterisation of PuPO$_4$: A potential analytical standard for EPMA actinide quantification. *IOP Conf Ser: Mater Sci Eng* **304**, 1–6.

Wright KE & van Rooyen IJ (2020). Fission product distribution in irradiated safety-tested and non-safety- tested AGR-2 TRISO particles fission product distribution in irradiated safety-tested and non-safety-tested AGR-2 TRISO particles. *IOP Conf Ser: Mater Sci Eng* **891**, 012024.